Enhanced SERS performance of gold nanoparticle assemblies on a cysteine-mutant Tobacco mosaic virus scaffold

Haziq Naseer Khan, Nathaly Ortiz-Pena, Cora Moreira da Silva, Stéphanie Lau-Truong, Guillaume Wang, Jakub Dusek, Leïla Boubekeur-Lecaque, Tomas Moravec, Damien Alloyeau, Nguyêt-Thanh Ha Duong

Journal of Science: Advanced Materials and Devices 9 (2024) 100775

Contents lists available at ScienceDirect

Journal of Science: Advanced Materials and Devices

journal homepage: www.elsevier.com/locate/jsamd

Research Article

Enhanced SERS performance of gold nanoparticle assemblies on a cysteine-mutant Tobacco mosaic virus scaffold

Haziq Naseer Khan [a], Nathaly Ortiz-Pena [b], Cora Moreira Da Silva [a], Stéphanie Lau-Truong [a], Guillaume Wang [b], Jakub Dusek [c], Leïla Boubekeur-Lecaque [a], Tomas Moravec [c], Damien Alloyeau [b], Nguyêt-Thanh Ha Duong [a,*]

[a] Université Paris Cité, ITODYS, CNRS, F-75013, Paris, France
[b] Université Paris Cité, CNRS, Laboratoire Matériaux et Phénomènes Quantiques, 75013, Paris, France
[c] Institute of Experimental Botany of the Czech Academy of Sciences, Prague 6, 160 00, Czech Republic

ARTICLE INFO

Keywords:
Plant virus
Plasmonic
In situ TEM
Self-assembly
Mineralization

ABSTRACT

The employment of biomolecular templates for the synthesizing nanohybrid constructs is expanding, driven by their prospective uses in biosensing and biomedical fields. Gold nanoparticles (AuNPs) and, in particular, their assemblies are especially preferred for Surface Enhanced Raman Spectroscopy (SERS) because of their ability to amplify Raman signals through localized surface plasmon resonances, thus enabling the detection of molecules at exceedingly low concentrations. Our investigative approach is dedicated to studing the role of cysteine mutants in the nucleation and assembly of AuNPs on Tobacco mosaic virus (TMV-C, carrying T158C mutation) scaffolds. Employing biomineralization and direct grafting methods, we synthesized these nanohybrids and examined them using conventional transmission electron microscopy (TEM), in situ liquid TEM, and fluorescence spectroscopy. We demonstrated that the syntheses obtained with TMV-C give denser plasmonic nanostructures, with is ideal for SERS applications. The SERS performances of these novel nanohybrids with various AuNPs sizes and densities were evaluated, revealing excellent enhancement factors for the nanosystems obtained by direct grafting that highlight their potential for the detection of biomolecules in solution.

1. Introduction

The use of biomolecular templates to prepare hybrid materials with a significant control over the spatial organization of metallic nanoparticles has emerged as a promising field that interconnects nanoscience with biotechnology. In recent times, the use of these biohybrid nanostructures has increased significantly, owing to their potential applications in biomedical imaging, drug delivery systems, biochemical sensing, and catalysis [1–4]. A promising approach has been to utilize plant virus capsids as templates for organizing 3D nano-objects, leading to the creation of novel functional nanomaterials. The nanotechnology field finds plant viruses fascinating owing to their symmetrical properties, versatility, consistent size distribution, and capacity for self-assembly [5,6].

Among many plant viruses, the Tobacco mosaic virus (TMV) has been widely studied due to its resilient nature to environmental changes (to both thermal and chemical treatments) and its ability to be modified with functional materials. The building blocks of TMV capsids consist of approximately 2130 uniform coat proteins arranged in a spiral pattern along a specific RNA strand. This arrangement forms a rod-like structure measuring 300 nm, with an outer width of 18 nm and an inner space that is 4 nm wide [7,8]. Its straightforward architecture likely contributes to its achievements, and its widespread accessibility has facilitated biochemical and structural investigations [9–12]. Several mutants with cysteine or lysine amino acids on the outer surface of TMV capsid have been made, offering rich surface chemistry and various potential functionalizations [11]. TMV is harmless to mammals, biodegradable, and therefore a potential candidate for applications in the biomedical field [13–15].

AuNPs exhibit unique plasmonic properties due to the localized surface plasmon resonance (LSPR) effect, where incident light induces electron oscillations on their surface, resulting among others, in a strong

Peer review under responsibility of Vietnam National University, Hanoi.
* Corresponding author.
E-mail address: thanh.haduong@u-paris.fr (N.-T. Ha Duong).

https://doi.org/10.1016/j.jsamd.2024.100775
Received 12 June 2024; Received in revised form 7 August 2024; Accepted 12 August 2024
Available online 13 August 2024

confinement of electric fields in the vicinity of nanoparticle surface [16, 17]. These properties enable their use in various biomedical applications including sensitive detection through surface-enhanced Raman spectroscopy (SERS) [18,19]. The plasmonic response of AuNPs, characterized mainly by absorption wavelength and enhancement factor, is tunable through their size, shape, and also by their assembly. Thanks to strong electromagnetic coupling, assemblies of multiple AuNPs create "hot spots" with amplified plasmonic effects, resulting in red shifts and broadening of the plasmon resonance [20]. In order to synthesize AuNPs assemblies as efficient plasmonic devices, several bottom-up strategies have been developed, often leading to arrangements of the NPs in 2D monolayers or aggregates [21–23]. Despite advancements in dimerization strategy [24,25], the reproducibility and the precise control over aggregate composition and interparticle spaces remain challenging for larger aggregates.

Many studies have been conducted on the attachment of metallic nanoparticles (NPs) to TMV in order to control their deposition and organization. Dujardin et al. used anionic metal precursors (e.g., $[AuCl_4]^-$, $[PtCl_6]^{2-}$) to graft NPs onto the outer surface of native TMV virus (TMV-wt) [26]. Lim et al. studied Au(III), Pd(II) and Au–Pd alloy biosorption on the genetically modified model biological template TMV [27,28]. More recently, through a multiscale study, joining liquid-cell transmission electron microscopy (LCTEM) and emission and absorption spectroscopies, we proposed a mechanism for the nucleation and growth of gold nanoparticles onto TMV-wt capsid, allowing the optimization and control of size and dispersity of the gold assembly [29].

The N-terminal threonine of TMV capsid protein is located on the outer surface of TMV capsid [30]. In this study, we then mutated this threonine into cysteine and investigated the use of mutated TMV (TMV-C) as a template for the synthesis of nanohybrids of AuNPs with a controlled size and morphology. The two methods used to deposit AuNPs onto TMV-C surface are: (1) Biomineralization which involves the reduction of Au^{3+} to Au^0 after the interaction of the gold salt with TMV-C (2) Direct grafting, when pre-formed gold nanoparticles are directly attached onto the surface of TMV-C. We studied the growth mechanism of NPs on TMV-C using liquid in situ TEM and fluorescence quenching experiments and compared the results to those obtained with the native TMV (TMV-wt). Additionally, we examined the plasmonic properties of TMV-C@AuNPs by performing SERS experiments with 1, 2-di(4-pyridyl)ethylene (BPE) as the reporter molecule. We demonstrated that the resulting TMV-C@AuNP nanohybrids have the potential to serve as an efficient and versatile nanotool for SERS applications, including the detection of biomolecules in solution.

2. Materials & methods

The generation, inoculation and purification of TMV-C were described in the Electronic Supplementary Material file. Tetrachloroaurate(III) acid hydrate $HAuCl_4.xH_2O$ (99.9 %), sodium borohydride (99 %) and trisodium citrate di-hydrate (citrate, 99%) were purchased from Alfa Aesar and used without further purification. Glacial acetic acid was purchased from VWR Chemicals. Dextran (average molecular mass of 67 100 Da) and 1,2-di(4-pyridyl)ethylene (BPE) were purchased from Sigma-Aldrich.

2.1. Biomineralization of AuNPs over TMV-C

The biomineralization protocol is inspired by the article by Moreira Da Silva et al. [29] In brief $HAuCl_4$ is sonicated with the solution of TMV-C for 15 min in acetic media (pH 2.4) and kept at room temperature for 2 h. Then $NaBH_4$ is added to reduce metallic cations followed by the quick addition of 1 ml ethanol to stop the reaction and prevent ripening phenomena. After the formation of gold seeds onto TMV-C, the size of AuNPs is increased by cyclic growth. First, 25 µl of $HAuCl_4$ (0.5 mM) were added and after 1 min, additional 50 µl of $NaBH_4$ (5 mM) were added in each cycle. For colloidal stability dextran (130 µl, 0.3 mg/ml) was added to the solution after the last cycle and sonicated for 30 min.

2.2. Direct grafting of AuNPs over TMV-C

The 10 and 16 nm AuNPs synthesis was adapted from Turkevich et al. [31] (Electronic Supplementary Material). The 5 nm AuNPs were purchased from Sigma-Aldrich. 1 ml of pre-formed AuNPs surrounded by citrate as surfactant (abs 0.7) was sonicated for 15 min with 15 µl TMV-C (0.2 mg/ml) solution and 100 µl of acetic acid (pH 3). After 1 h of incubation, 130 µl of dextran (0.3 mg/ml) was added as coating agent and sonicated for another hour. To remove the free AuNPs, the samples were passed through membrane (MWCO 1 000 000 Da) with centrifugation at 2000 rpm for 8 min.

2.3. Characterization of the nanohybrids

UV–Visible spectra were recorded with Cary 4000 spectrophotometer using 10 mm path length quartz cuvettes. Fluorescence Spectroscopy (Fluorolog HORIBA JOBIN YVON) was used to determine the association constant between the TMV-C and $HAuCl_4$. Ex situ TEM imaging of the NPs was carried out using a JEOL 2100 Plus microscope operating at 200 kV. To prepare the samples for TEM analysis, 5 µL of the nanohybrid solution was dropped on a carbon-coated copper grid. In-situ liquid TEM was performed on an aberration-corrected JEOL ARM 200F microscope operating in STEM mode at 200 KV using a liquid-cell TEM holder from Protochips. The protocol of these LCTEM investigations of AuNP growth over the TMV-C (see SI) was previously developed to study the growth of AuNPs on TMV-wt [29].

Samples for SERS measurements were prepared by mixing 5 µL of BPE at various concentrations (BPE was first dissolved in Ethanol at 10^{-1} M, and then diluted in water at the corresponding concentration, from 10^{-3} to 10^{-7} M) and 45 µL of a solution of nanobiohybrid with an absorbance of 0.7. This solution was analyzed in a cuvette of 2 mm optical path. Raman spectra were recorded using a confocal Raman microspectrometer Jobin-Yvon LABRAM HR 800 equipped with a thermoelectric cooled CCD and a motorized XY displacement stage. In the present study, a continuous wave (CW) 633 nm He–Ne laser was used for SERS excitation. The laser line (output power 5 mW) was focused onto samples through a long working distance ×10 objective (0.25 N A) and the Rayleigh scattering signal collected through the same objective in backscattering mode. The scattered light (accumulation time 5 s, three repetitions) was filtered with a long pass edge filter.

3. Results and discussion

3.1. Spectrophotometric titration of $HAuCl_4$ binding to TMV-C

To determine the affinity constant of gold complex to TMV-C subunit (Equation (1)), fluorescence experiments were performed by exciting the virus capsid at 280 nm. The addition of an increasing amount of $HAuCl_4$ to a solution of TMV-C in acidic media (pH 2.4) leads to a decrease of the fluorescence emission without any spectral shift (Fig. 1A). This quenching was analyzed at 316 nm using a modified Stern-Volmer equation (Equation (2)). From the intercept and slope of Fig. 1B, $\mathrm{Log}K_a$ and n values were found to be 5.95 ± 0.15 and 1.2 ± 0.1, respectively. The n value indicates the stoichiometry of the interaction between $HAuCl_4$ and one subunit of TMV-C capsid. The affinity constant value is 10 fold higher than that of TMV-wt determined previously ($\mathrm{Log}K_a = 4.80 \pm 0.05$) [29]. Indeed, given its isoelectric point (pI) value (around 3.5 and 4.6) [32], the outer surface of TMV-wt is positively charged at pH 2.4. Therefore, the negative gold salt $[AuCl_4]^-$ interacts with TMV-wt capsid by electrostatic interaction, whereas gold atoms can form a stronger covalent bond with TMV-C thanks to the presence of cysteine thiol groups [33].

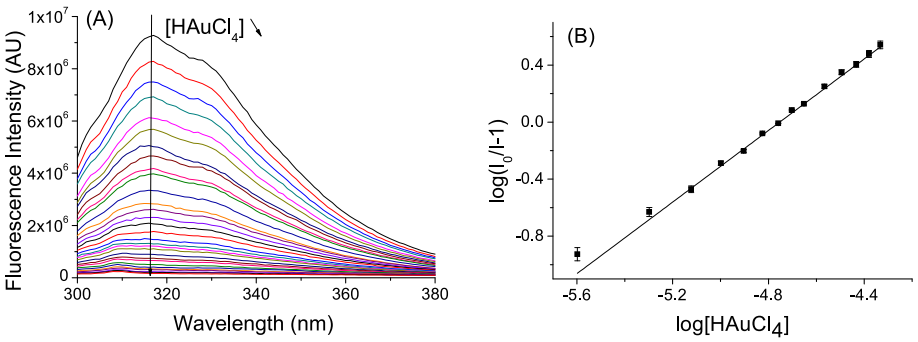

Fig. 1. (A) Emission spectra (λ_{exc} = 280 nm) of TMV-C (0.1 mg/mL) in acetic acid 5% (pH = 2.4) at different concentrations of $HAuCl_4$ (0–50 μM) and (B) modified Stern-Volmer plot.

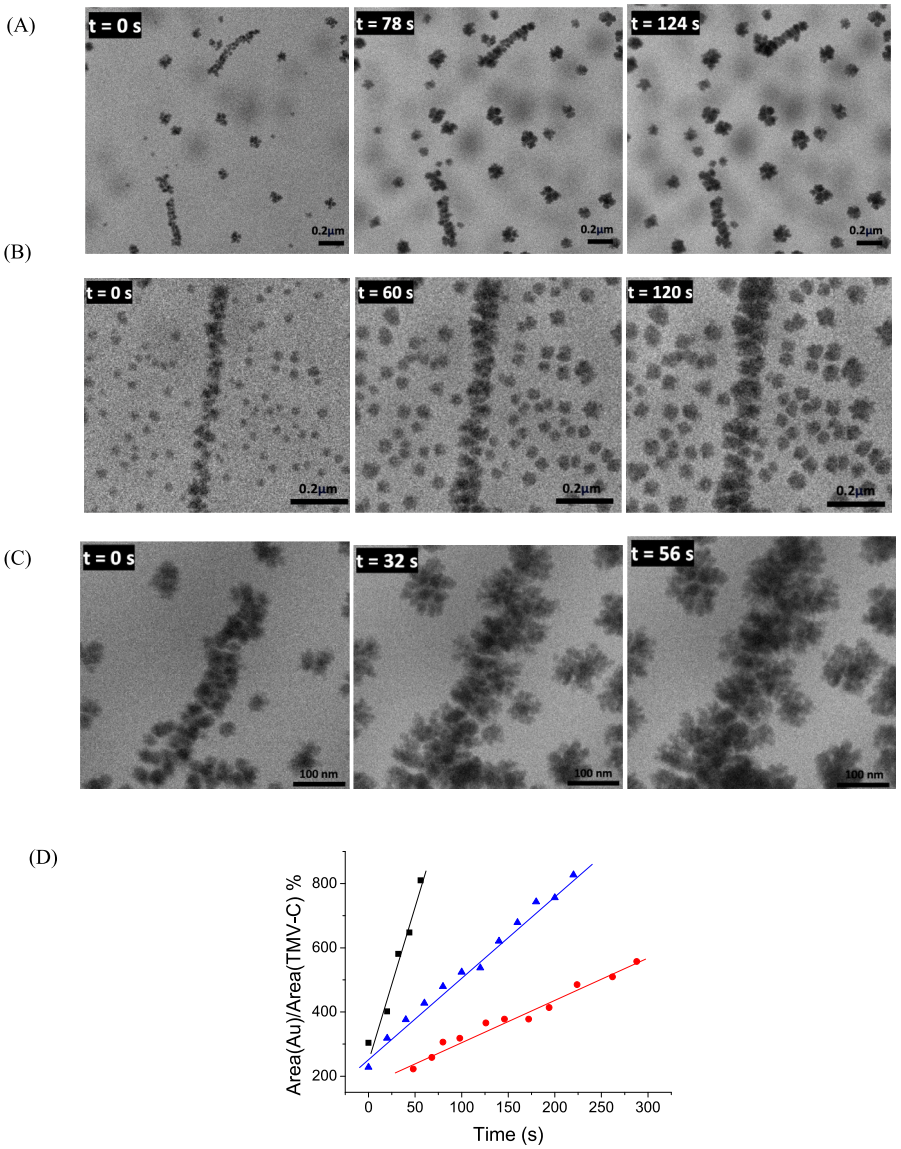

Fig. 2. STEM bright field image series of AuNPs growth on TMV-C with an electron dose rate of (A) 0.14 e^-/A^2 s, (B) 0.55 e^-/A^2 s, and (C) 2.2 e^-/A^2 s. The acquisition time is indicated in the left corner of each image. (D) Total projected surface area of AuNPs normalized by the projected surface area of TMV-C as a function of time for the three different electron dose rates: 0.14 e^-/A^2 s (in red), 0.55 e^-/A^2 s (in blue) and 2.2 e^-/A^2 s (in black).

$$\text{subTMV} - \text{C} + \text{n HAuCl}_4 \rightarrow \left[\text{subTMV} - \text{C} - (\text{HAuCl}_4)_n\right] \quad (1)$$

where subTMV-C is a subunit of the capsid, and the affinity constant is expressed as $K_a = [\text{subTMV-C-(HAuCl}_4)_n]/[\text{subTMV-C}][\text{HAuCl}_4]^n$

$$\log\left(\frac{I_0 - I}{I}\right) = \log K_a + n\log[HAuCl_4] \quad (2)$$

3.2. In situ TEM

In situ TEM observations were then performed to measure the influence of cysteine on the growth rate of AuNPs. LCTEM has emerged as a widely adopted in situ methodology for directly observing the nucleation and growth of metal nanoparticles (NPs) in liquid environment [34], including interfacial reactions on biological surfaces such as bacteria [35], vesicles [36,37] and more recently viruses [29]. Therefore, biomineralization experiments were conducted under the same experimental conditions as those used with TMV-wt [29]. Briefly, after 2 h of incubation, a solution containing TMV-C (0.2 mg mL^{-1}) and $HAuCl_4$ (1 mM) in 5% acetic acid was loaded into the TEM liquid cell. Gold salt dissolved in 5% acetic acid (1 mM) was continuously injected into the liquid cell during acquisition. The reduction reaction was driven by water radiolysis induced by the electron beam [38,39]. Three different electron dose rates (0.14 $e-/A^2$ s, 0.55 $e-/A^2$ s and 2.20 $e-/A^2$ s) were used to study the growth rate of NPs as a function of the concentration of reducing agents. In Fig. 2, the STEM images show the growth of AuNPs occurs both on the SiN window of the liquid cell and TMV-C. As previously observed, the density of AuNPs is much lower in the SiN membrane than on TMV capsid [29], because of the high affinity of the gold precursors for the virus surface. This is especially true of the TMV-C on which the density of NPs is several orders of magnitude higher than on the window. Moreover, the biomineralization only occurs on the outer surface of the capsid. Indeed, TMV-C consists of the mutation of the C-terminal threonine to cysteine. Both residues are non-charged, so we assume that the isoelectric point of TMV-C is similar to that of TMV-wt. Therefore, at acidic pH, charge of the inner cavity approaches neutrality, while the outer surface exhibits a positive charge [26,32]. Hence, the outer surface of the TMV cylinder is expected to be the primary site for adsorption, thanks to electrostatic interaction between the positively charged TMV-C and the negatively charged gold complex $[AuCl_4]^-$ as well as the presence of thiol allowing Au–S covalent bond. Fig. 2D shows that the total projected surface area of AuNPs normalized by the projected surface area of TMV-C increases linearly with time. The growth rate of gold NPs deduced from the slope of the linear fit of the curves, increases with the electron dose rate. More importantly, at each electron dose rate, the growth rate of NPs is higher on TMV-C than on TMV-wt (Table 1). The nucleation and growth mechanisms of AuNPs are similar on TMV-wt and TMV-C [29]. At first, gold precursors bind to the virus surface. Then, the reduction of $HAuCl_4$ drives the nucleation and growth of NPs by monomer attachment on the capsid and finally coalescence phenomena rapidly occur when the NPs get in contact. As the binding affinity of gold precursors is higher for TMV-C than for TMV-wt, the higher reduction rate measured on TMV-C is very likely due to the higher concentration of $HAuCl_4$ on the virus capsid.

3.3. Biomineralization

We also carried out beaker-scale biomineralization experiments to compare the formation dynamics of gold NPs on TMV-wt and TMV-C.

Table 1
Rate of AuNP growth. Slope of area(Au)/Area(TMV-C) against time in %/s.

e^- dose rate (e^-/A^2 s)	0.14	0.55	2.2
TMV-wt [29]	1.12 ± 0.10	1.75 ± 0.16	3.53 ± 0.32
TMV-C	1.28 ± 0.07	2.59 ± 0.08	9.1 ± 1.0

After 2 h incubation of TMV (0.2 mg/mL) with $HAuCl_4$ (0.5 mM) and 15 min of ultrasonic bath, $NaBH_4$ (5 mM) is added to form a high density of seeds at the surface of TMV-C. Then, four sequential injections of $HAuCl_4$ (0.5 mM) and $NaBH_4$ (5 mM) were performed to drive a slow growth phase minimizing NP coalescence. Besides providing a great control over the nucleation and growth processes, this protocol with several reduction cycles allows studying the size distribution and density of NPs by TEM after each cycle. Fig. 3 shows that the seed size after the first cycle is lower on TMV-wt than on TMV-C (2.4 nm and 6.3 nm, respectively). As observed by liquid-cell TEM, the coalescence-driven growth processes are thus faster on TMV-C, which explains the higher density of NPs on TMV-wt than on TMV-C (3.3 *10^{-2} NP/nm^2 and 2.1 × 10^{-2} NP/nm^2, respectively). This tendency is also observed during the subsequent reduction cycles since the average size of NPs on TMV-wt increased from 2.4 nm to 5.8 nm in after five cycles, while the NPs on TMV-C enlarged from 6.3 to 12.4 nm. After 5 cycles, NP density reaches similar values for both viruses (1.5 and 1.3 × 10^{-3} NP/nm^2 for TMV-wt and TMV-C, respectively) but remains higher with a more uniform NP size compared to the method described by Lim et al. [27,28]. Some free AuNPs were also observed after each cycle due to the non-bounded gold precursors to the capsid which gets reduced to gold nanoparticles on addition of $NaBH_4$ (Fig. 3A), as already described by Dujardin et al. [26]. Nevertheless, the presence of free NPs was significantly lower when using TMV-C. The results of these beaker-scale syntheses confirm the conclusion of spectrophotometry and in situ TEM experiments: the higher affinity of gold precursors for the external capsid of TMV-C leads to faster growth processes than on TMV-wt. The gold nanoparticles grafted through biomineralization on TMV-C were characterized using transmission electron microscopy (TEM), and energy dispersive X-ray spectroscopy (EDX) (Fig. 3C and D).

From cycle 1 to 4, the absorbance of plasmonic band increases with the number of reduction cycles (Fig. 4) confirming the formation and growth of plasmonic nanostructures on the surface of TMV-C. The cycle 1 spectrum of TMV-C shows a maximum at 535 nm, which is close to the value found after 5 cycles of biomineralization on TMV-wt [29]. Indeed, the similar wavelength could be explained by AuNPs of comparable size (8 nm and 6.3 nm for cycle 5 on TMV-wt and cycle 1 on TMV-C respectively). After 5 cycles, a red shift is observed from 535 to 541 nm, due to the higher diameter of AuNP on the surface [40]. As previously observed with TMV-wt, the plasmonic band is red-shifted and broader compared to AuNPs alone (Fig. 4) due to the plasmonic interactions that occur when nanoparticles are in close proximity to each other. Despite the low absorbance of the plasmonic band, the size and uniformity of AuNPs as well as their density on TMV-C are well-adapted to perform SERS experiments. To increase their stability, Dextran is added to the solution. Additionally, these nanoparticles are water-soluble, making them suitable for use as sensors in solutions.

3.4. Direct grafting

To obtain nanohybrids materials with higher plasmonic absorbance, we synthesized TMV-C@AuNP by directly grafting pre-formed AuNPs to the outer surface of the capsid at pH 3. The addition of small volumes of TMV-C to a solution of AuNPs of 10 nm in diameter reduces the intensity of the absorption spectra (Fig. 5A) with a red shift of the plasmon band (from 521 to 526 nm) and exposes an isobestic point at 566 nm, revealing the existence of equilibrium between two absorbing species, namely free AuNPs and grafted AuNP on TMV-C. In the case of 16 nm AuNPs, we observed a decrease in absorbance of the plasmon band without any spectral shift but an increase of shoulder located beyond the isobestic point at 591 nm (Fig. 5B). These observations strongly imply an interaction between sulfur atoms of TMV-C and AuNP surfaces [41]. Subsequently, after a filtration step which is necessary to remove free AuNP (ESM, Fig. S1), TEM images portray TMV-C surfaces coated with 10 nm and 16 nm AuNPs (Fig. 5C and D). As expected, the densities on TMV-C decrease with the AuNP diameter, from 11.5 × 10^{-3} NP/nm^2 for

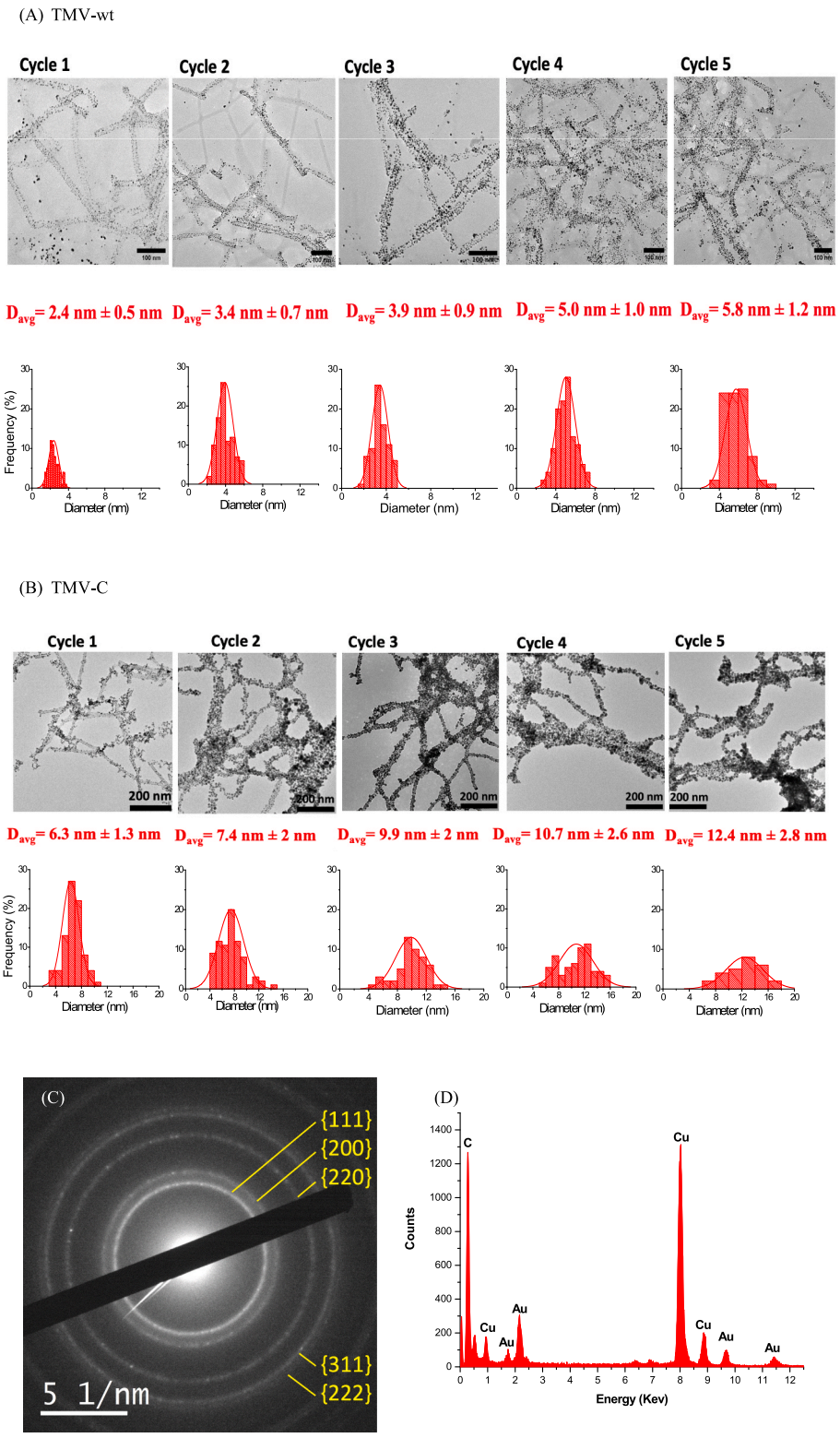

Fig. 3. Biomineralization synthesis at the beaker-scale. TEM images, mean size (D_{avg}) and size distribution graphs of AuNPs after each reduction cycle on (A) TMV-wt and (B) TMV-C. (C) Electron diffraction pattern from the AuNPs after biomineralization on TMV-C showing the (111), (200), (220), (311), and (222) reflections of AuNP. (D) EDX spectrum of gold nanoparticles (Cu signals comes from the copper grid).

10 nm to 8.16×10^{-3} NP/nm^2 for 16 nm. The density for direct grafting was 6–8 times higher than that observed after the fifth cycle of biomineralization (1.3×10^{-3} NP/nm^2). Consequently, the AuNPs are more closely packed on the TMV surface, potentially creating a larger number of hot spots to could enhance the SERS signal. The same protocol was also performed with TMV-wt and after filtration, only few 10 nm AuNPs were attached to the outer surface of TMV-wt (Fig. S2). This confirms the major role of cysteine in forming stronger bond between AuNPs and TMV-C. The same experiments are repeated with pre-formed 5 nm AuNPs. The changes in absorption spectra are much smaller even if an

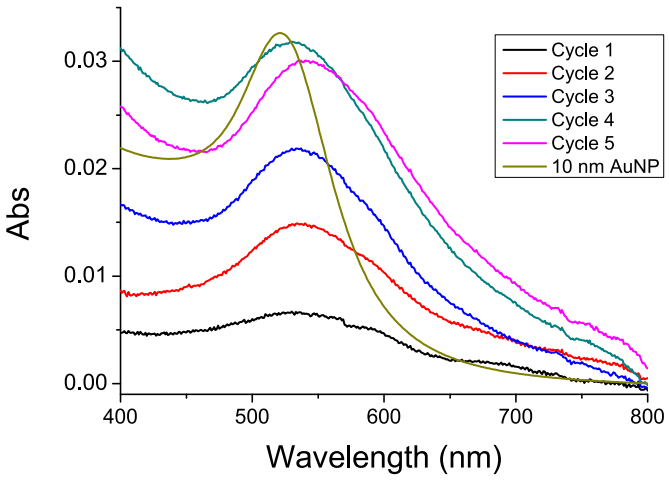

Fig. 4. Absorption spectra of gold-coated TMV-C after each reduction cycle.

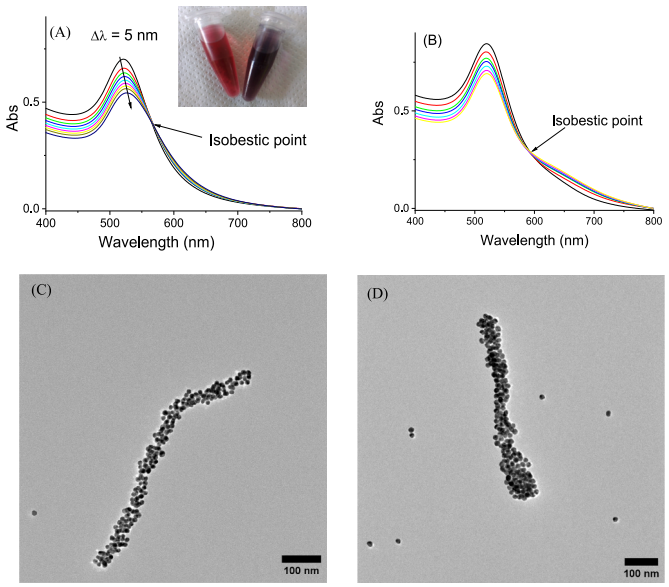

Fig. 5. Absorption spectra of (A) 10 nm or (B) 16 nm AuNPs with increasing concentrations of TMV-C (from 0 to 14 μLat 0.2 mg/mL). The picture in insert shows colloid solutions of 10 nm AuNP alone (left) and grafted onto TMV-C (right). TEM images of (C) 10 nm or (D) 16 nm AuNPs grafted onto TMV-C.

isobestic point is evidenced at 553 nm (Fig. S3A). After the grafting of 5 nm AuNPs onto TMV, TEM images showed that the AuNP are not juxtaposed (Fig. S3B), despite the density of 14 × 10^{-3} NP/nm^2 on TMV-C.

3.5. SERS

The nanohybrids were tested for surface-enhanced Raman spectroscopy (SERS) using 1,2-di(4-pyridyl)ethylene (BPE) as a molecular probe. In the presence of bare TMV-C, the Raman bands in the solution of BPE were not observed, as previously described for Turnip yellow mosaic virus (TYMV) (Fig. S4) [42]. To conduct a comparative analysis, we employed solutions exhibiting equivalent absorbance values at the plasmon band (0.7 abs). With AuNPs alone (Fig. 6A), the Raman spectra of BPE exhibited characteristic peaks at 1000 cm^{-1}, 1200 cm^{-1}, 1610 cm^{-1} and 1639 cm^{-1}. These peaks correspond to the vibrational modes associated with pyridine breathing, in-plane ring, aromatic stretching and C═C stretching modes, respectively. In case of nanohybrids

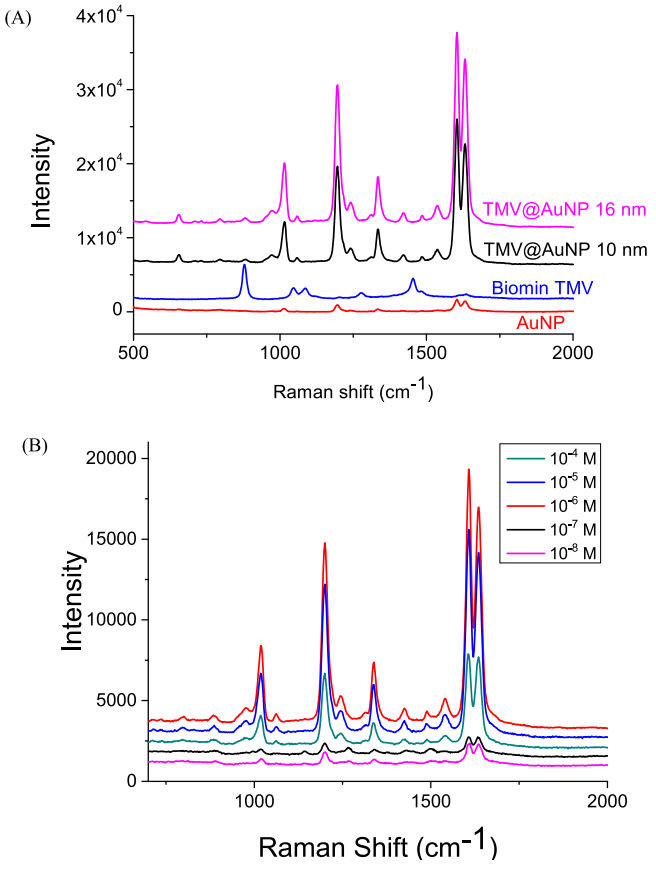

Fig. 6. SERS experiments. Raman spectra of BPE (A) at 10^{-6} M in solution in the presence of 10 nm AuNP (red), biomineralized TMV (blue), TMV-C@AuNP-10 nm (black) and TMV-C@AuNP-16 nm (pink), and (B) at different concentrations in the presence of TMV@AuNP-16 nm. The spectra are vertically shifted for clarity.

prepared by biomineralization, we had used the concentration of $HAuCl_4$ at 5 mM during the cyclisation steps to increase the absorbance of plasmon band. However, the sizes of AuNPs on TMV-C were heterogenous (Fig. S5). Moreover, the major bands in the presence of biomineralized material could be attributed to ethanol, used during the biomineralization process. Indeed, the Raman spectra of the biomineralized nanohybrid without BPE shows identical peaks (Fig. S6), and the characteristic bands of BPE (in particular 1200 cm^{-1}, 1610 cm^{-1} and 1639 cm^{-1}) are barely noticeable with much lower intensity than with AuNPs at the same concentration of BPE (Fig. 6A). These low SERS performances are very likely due to precipitation of the nanohybrid synthesized by biomineralization method. Fig. 6A also shows the enhancement in intensity of Raman peaks in the presence of TMV-C@AuNPs prepared by grafting method, for AuNPs size of 10 nm, which was not observed in case of TYMV [42]. Indeed, for icosahedral virus, only few nanoparticles were grafted onto the outer surface, and the interparticle distance is too large and local electric field intensity is supposed to be not enough to enhance the Raman signals during SERS experiments. However, thanks to its rod-like structure of 300 nm, TMV-C@AuNP shows many AuNPs grafted at its surface and many of them are juxtaposed and probably create hot junction spots. The same experiment was repeated with the nanohybrid synthetized seven days earlier, indicating the stability of the nanohybrid and reproducibility of the SERS experiments (Fig. S7).

The effect of AuNP size on the solution-based SERS signal was also investigated. No Raman bands of BPE were observed in the presence of TMV@AuNP of 5 nm (Fig. S8), probably because the small-sized nanoparticles feature a weak confinement of electric field [43] and the large

interparticle separation once grafted on TMV-C does not favor electromagnetic coupling (Fig. S3B). It was found that nanohybrids with 16 nm AuNPs exhibited higher signal intensity compared to those with 10 nm particles (Fig. 6A). For such medium sized nanoparticles (10–100 nm), it is well established that the quality factor of the localized surface plasmon resonance increases with the diameter of spherical particles leading to stronger electric field enhancement. Besides, for a given excitation wavelength, the penetration depth which refers to the extent to which the confined electromagnetic field penetrates into the surrounding medium, increases with the size of the plasmonic nanoparticle. The penetration depth has a critical influence on the coupling between two closely spaced nanoparticles.

Interestingly, the intensity of the characteristic Raman bands of BPE in the presence of nanohybrids TMV-C@AuNP-16 nm, shows a non-monotonous behavior for concentrations ranging from 10^{-8} to 10^{-4} M (Fig. 6B and S9). As for TMV-C@AuNP-10 nm, the band intensities increased with the concentration of BPE (from 10^{-8} to 10^{-6} M, Fig. S10), and then decreased. This may be explained by the bidentate character of BPE with two nitrogen donors able to form molecular junction between two neighboring AuNPs [24]. Indeed, Fig. S11 shows UV–visible absorption spectra of TMV-C@AuNP-16 nm at different concentration of BPE (ranging from 10^{-6} to 10^{-4} M). In the absence of BPE, the absorption spectrum shows a strong band at 521 nm originating from the LSPR of grafted but non interacting AuNPs on TMV-C. An additional small band located at 613 nm can be evidenced which is assigned to coupled AuNPs grafted on the TMV-C surface. At low concentration and up to 10^{-6} M of BPE in solution, the absorption spectrum reveal a remarkable increase of the coupling band at 613 nm, and the concomitant decrease of the characteristic band at 521 nm of TMV-C@AuNP-10 nm. The relative intensities of these two bands are strongly impacted by the concentration of BPE in the medium. Beyond the critical concentration of 10^{-6} M of BPE, the coupling band tends to decrease whereas the other band increases. It appears that low concentrations of BPE favor the coupling of AuNPs whereas high concentrations of BPE tend to separate AuNPs. Such dimerization process between nanoparticles may involve AuNPs grafted on two distinct virus TMV-C (inter-virus dimerization leading ultimately to aggregation) or very close AuNPs grafted on the same virus TMV-C (intra-virus dimerization). It is important to mention that the colloidal suspension is stable over time for at least 24h (Figs. S12A and S12B), and TEM images indicated no dimerization of TMV-C regardless of BPE concentration (Fig. S12C) which rules out the inter-virus dimerization possibility. Therefore, the BPE induced-coupling of AuNPs revealed by these experiments (coupling band at 613 nm) is more likely due to the intra-virus dimerization of closely spaced AuNPs. At low BPE concentration, free spaces likely remain available on gold surface to create BPE molecular junction with another AuNPs. Conversely, at high BPE concentration, gold surface being saturated with BPE molecules, the dimerization of nanoparticles becomes very unlikely. Following this line of reasoning, with less hot spots, the Raman signal is expected to decrease at high concentration of BPE.

The analytical enhancement factor (AEF) was calculated by using Equation (3) for AuNPs of 10 and 16 nm, either free in solution or grafted onto TMV-C [44].

$$AEF = \frac{(I_{SERS}/C_{SERS})}{(I_{RS}/C_{RS})} \quad (3)$$

Where I_{SERS} and I_{RS} are the signal intensities under SERS and non-SERS conditions measured at the same excitation wavelength and conditions of acquisition and where the concentration in solution of BPE is C_{SERS} (10^{-6} M) and C_{RS} (10^{-1} M) respectively.

The AEF values for 10 nm or 16 nm AuNPs in solution were similar (0.14 and 0.12 $\times$ 10^5, respectively), but those for TMV-C@AuNPs nanohybrid are 14 and 23 times higher, respectively (Table 2). Indeed, it was already reported that assemblies of gold nanoparticles presented higher enhancement [45]. These AEF values are excellent for SERS substrates in solution. They were also more significant than the ones of nanohybrid made from AuNPs with Turnip yellow mosaic virus (TYMV) as reported by the Nguyen et al. [42]. This increase can be associated with the higher number of plasmonic hotspots or density of AuNPs on the surface of the TMV-C.

Table 2
Analytical enhancement factors in solution of nanohybrids and free AuNPs.

	AEF
TMV-C@AuNPs (16 nm)	$(2.8 \pm 0.1) \times 10^5$
AuNPs (16 nm)	$(0.12 \pm 0.02) \times 10^5$
TMV-C@AuNPs (10 nm)	$(2.0 \pm 0.1) \times 10^5$
AuNPs (10 nm)	$(0.14 \pm 0.03) \times 10^5$

4. Conclusion

The study showed the impact of cysteine on AuNP nucleation in TMV-based nanohybrids, targeting advancements in Surface-Enhanced Raman Scattering (SERS) applications. By employing both biomineralization and direct grafting techniques, we were successful in synthesizing TMV-C@AuNP nanohybrids with varied AuNP sizes. Notably, the association constant (K_a) for $HAuCl_4$ with mutated TMV-C, determined via fluorescence quenching methods, was significantly higher compared to the wild-type TMV. Additionally, the growth rate of AuNPs, assessed through in situ liquid Transmission Electron Microscopy (TEM), was markedly higher on the TMV-C variant, thus enabling the synthesis of a plasmonic nanohybrid featuring a uniform distribution of approximatively 10 nm AuNPs on the TMV-C capsid by biomineralization method. The presence of cysteine residues on the capsid surface facilitated the assembly of 10 nm and 16 nm AuNPs via direct grafting, producing a soluble plasmonic nanostructure with high optical absorption. SERS analysis of these nanohybrids, particularly those created through direct grafting, showed increased signaling with BPE molecules, highlighting their potential as effective biosensing tools. This work not only contributes to the development of new materials and strategies for enhancing SERS analysis but also demonstrates the potential of using mutated viruses with metallic nanoparticles to design innovative bifunctional nanomaterials. These findings have significant implications for biosensing and biomedicine and could inspire similar approaches across various scientific domains.

Conflicts of interest

The authors declare no conflicts of interest.

CRediT authorship contribution statement

Haziq Naseer Khan: Writing – original draft, Visualization, Investigation. **Nathaly Ortiz-Pena:** Investigation. **Cora Moreira Da Silva:** Writing – review & editing, Investigation. **Stéphanie Lau-Truong:** Investigation. **Guillaume Wang:** Investigation. **Jakub Dusek:** Investigation. **Leïla Boubekeur-Lecaque:** Writing – review & editing. **Tomas Moravec:** Writing – review & editing, Resources. **Damien Alloyeau:** Writing – review & editing, Conceptualization. **Nguyêt-Thanh Ha Duong:** Writing – review & editing, Writing – original draft, Validation, Investigation, Conceptualization.

Declaration of competing interest

The authors declare that they have no known competing financial interests or personal relationships that could have appeared to influence the work reported in this paper.

Acknowledgment

ANR (Agence Nationale de la Recherche) and CGI (Commissariat à l'Investissement d'Avenir) are gratefully acknowledged for their financial support of this work through Labex SEAM (Science and Engineering for Advanced Materials and devices), ANR-10-LABX-0096 and ANR-18-IDEX-0001. T.M. and J.D. were supported by the mobility grant "Nanomaterials based on Tobacco mosaic virus" Nr 8J24FR014 from the Ministry of Education, Youth and Sports of CR and by grant Nr: TM04000026 from Technology Agency of the Czech Republic.

Appendix A. Supplementary data

Supplementary data to this article can be found online at https://doi.org/10.1016/j.jsamd.2024.100775.

References

[1] M.-Q. He, Y.-L. Yu, J.-H. Wang, Biomolecule-tailored assembly and morphology of gold nanoparticles for LSPR applications, Nano Today 35 (2020) 101005, https://doi.org/10.1016/j.nantod.2020.101005.
[2] X. Ma, X. Li, G. Luo, J. Jiao, DNA-functionalized gold nanoparticles: modification, characterization, and biomedical applications, Front. Chem. 10 (2022). https://www.frontiersin.org/articles/10.3389/fchem.2022.1095488. (Accessed 15 January 2024).
[3] I. Capek, Viral nanoparticles, noble metal decorated viruses and their nanoconjugates, Adv. Colloid Interface Sci. 222 (2015) 119–134, https://doi.org/10.1016/j.cis.2014.04.008.
[4] F. Li, Q. Wang, Fabrication of nanoarchitectures templated by virus-based nanoparticles: strategies and applications, Small 10 (2014) 230–245, https://doi.org/10.1002/smll.201301393.
[5] Z. Liu, J. Qiao, Z. Niu, Q. Wang, Natural supramolecular building blocks: from virus coat proteins to viral nanoparticles, Chem. Soc. Rev. 41 (2012) 6178–6194, https://doi.org/10.1039/C2CS35108K.
[6] J.N. Culver, A.D. Brown, F. Zang, M. Gnerlich, K. Gerasopoulos, R. Ghodssi, Plant virus directed fabrication of nanoscale materials and devices, Virology 479–480 (2015) 200–212, https://doi.org/10.1016/j.virol.2015.03.008.
[7] J.M. Alonso, M.Ł. Górzny, A.M. Bittner, The physics of tobacco mosaic virus and virus-based devices in biotechnology, Trends Biotechnol. 31 (2013) 530–538, https://doi.org/10.1016/j.tibtech.2013.05.013.
[8] B.D. Harrison, T.M.A. Wilson, A. Klug, The tobacco mosaic virus particle: structure and assembly, Philos. Trans. R. Soc. Lond. B Biol. Sci. 354 (1999) 531–535, https://doi.org/10.1098/rstb.1999.0404.
[9] M.A. Bruckman, A.E. Czapar, A. VanMeter, L.N. Randolph, N.F. Steinmetz, Tobacco mosaic virus-based protein nanoparticles and nanorods for chemotherapy delivery targeting breast cancer, J. Controlled Release 231 (2016) 103–113, https://doi.org/10.1016/j.jconrel.2016.02.045.
[10] Z. Shan, H. Bi, A. Suonan, Y. Gu, H. Zhou, K. Xi, R. Xiong, H. Chen, L. Chen, Tobacco mosaic viral nanoparticle inhibited osteoclastogenesis through inhibiting mTOR/AKT signaling, Int. J. Nanomedicine 15 (2020) 7143–7153, https://doi.org/10.2147/IJN.S245870.
[11] G.P. Lomonossoff, C. Wege, Chapter six - TMV particles: the journey from fundamental studies to bionanotechnology applications, in: P. Palukaitis, M. J. Roossinck (Eds.), Adv. Virus Res., Academic Press, 2018, pp. 149–176, https://doi.org/10.1016/bs.aivir.2018.06.003.
[12] M. Hema, G.P. Vishnu Vardhan, H.S. Savithri, M.R.N. Murthy, Chapter 6 - emerging trends in the development of plant virus-based nanoparticles and their biomedical applications, in: V. Buddolla (Ed.), Recent Dev. Appl. Microbiol. Biochem., Academic Press, 2019, pp. 61–82, https://doi.org/10.1016/B978-0-12-816328-3.00006-4.
[13] Y.H. Chung, H. Cai, N.F. Steinmetz, Viral nanoparticles for drug delivery, imaging, immunotherapy, and theranostic applications, Adv. Drug Deliv. Rev. 156 (2020) 214–235, https://doi.org/10.1016/j.addr.2020.06.024.
[14] S. Shukla, H. Hu, H. Cai, S.-K. Chan, C.E. Boone, V. Beiss, P.L. Chariou, N. F. Steinmetz, Plant viruses and bacteriophage-based reagents for Diagnosis and Therapy, Annu. Rev. Virol. 7 (2020) 559–587, https://doi.org/10.1146/annurev-virology-010720-052252.
[15] C.I. Nkanga, N.F. Steinmetz, The pharmacology of plant virus nanoparticles, Virology 556 (2021) 39–61, https://doi.org/10.1016/j.virol.2021.01.012.
[16] M.-C. Daniel, D. Astruc, Gold nanoparticles: assembly, supramolecular chemistry, quantum-size-related properties, and applications toward biology, catalysis, and nanotechnology, Chem. Rev. 104 (2004) 293–346, https://doi.org/10.1021/cr030698+.
[17] J. Liu, H. He, D. Xiao, S. Yin, W. Ji, S. Jiang, D. Luo, B. Wang, Y. Liu, Recent Advances of plasmonic nanoparticles and their applications, Materials 11 (2018) 1833, https://doi.org/10.3390/ma11101833.
[18] R. Pilot, R. Signorini, C. Durante, L. Orian, M. Bhamidipati, L. Fabris, A review on surface-enhanced Raman scattering, Biosensors 9 (2019) 57, https://doi.org/10.3390/bios9020057.
[19] J. Langer, D. Jimenez de Aberasturi, J. Aizpurua, R.A. Alvarez-Puebla, B. Auguié, J. J. Baumberg, G.C. Bazan, S.E.J. Bell, A. Boisen, A.G. Brolo, J. Choo, D. Cialla-May, V. Deckert, L. Fabris, K. Faulds, F.J. García de Abajo, R. Goodacre, D. Graham, A. J. Haes, C.L. Haynes, C. Huck, T. Itoh, M. Käll, J. Kneipp, N.A. Kotov, H. Kuang, E. C. Le Ru, H.K. Lee, J.-F. Li, X.Y. Ling, S.A. Maier, T. Mayerhöfer, M. Moskovits, K. Murakoshi, J.-M. Nam, S. Nie, Y. Ozaki, I. Pastoriza-Santos, J. Perez-Juste, J. Popp, A. Pucci, S. Reich, B. Ren, G.C. Schatz, T. Shegai, S. Schlücker, L.-L. Tay, K. G. Thomas, Z.-Q. Tian, R.P. Van Duyne, T. Vo-Dinh, Y. Wang, K.A. Willets, C. Xu, H. Xu, Y. Xu, Y.S. Yamamoto, B. Zhao, L.M. Liz-Marzán, Present and Future of surface-enhanced Raman scattering, ACS Nano 14 (2020) 28–117, https://doi.org/10.1021/acsnano.9b04224.
[20] L. Litti, M. Meneghetti, Predictions on the SERS enhancement factor of gold nanosphere aggregate samples, Phys. Chem. Chem. Phys. 21 (2019) 15515–15522, https://doi.org/10.1039/C9CP02015B.
[21] B. Tim, P. Błaszkiewicz, M. Kotkowiak, Recent Advances in metallic nanoparticle assemblies for surface-enhanced spectroscopy, Int. J. Mol. Sci. 23 (2022) 291, https://doi.org/10.3390/ijms23010291.
[22] J. Pillanagrovi, S. Dutta-Gupta, Controlled assembly of gold nanoparticles in resonant gold nanoapertures for SERS applications, Nanotechnology 33 (2022) 485301, https://doi.org/10.1088/1361-6528/ac8c49.
[23] D. Zhang, L. Tang, J. Chen, Z. Tang, P. Liang, Y. Huang, M. Cao, M. Zou, D. Ni, J. Chen, Z. Yu, S. Jin, Controllable self-assembly of SERS hotspots in liquid environment, Langmuir 37 (2021) 939–948, https://doi.org/10.1021/acs.langmuir.0c03323.
[24] I. Haidar, G. Lévi, L. Mouton, J. Aubard, J. Grand, S. Lau-Truong, D.R. Neuville, N. Félidj, L. Boubekeur-Lecaque, Highly stable silica-coated gold nanorods dimers for solution-based SERS, Phys. Chem. Chem. Phys. 18 (2016) 32272–32280, https://doi.org/10.1039/C6CP06218K.
[25] J.H. Yoon, F. Selbach, L. Schumacher, J. Jose, S. Schlücker, Surface plasmon coupling in dimers of gold nanoparticles: experiment and theory for ideal (spherical) and Nonideal (Faceted) building blocks, ACS Photonics 6 (2019) 642–648, https://doi.org/10.1021/acsphotonics.8b01424.
[26] E. Dujardin, C. Peet, G. Stubbs, J.N. Culver, S. Mann, Organization of metallic nanoparticles using tobacco mosaic virus templates, Nano Lett. 3 (2003) 413–417, https://doi.org/10.1021/nl034004o.
[27] J.-S. Lim, S.-M. Kim, S.-Y. Lee, E.A. Stach, J.N. Culver, M.T. Harris, Quantitative study of Au(III) and Pd(II) ion biosorption on genetically engineered Tobacco mosaic virus, J. Colloid Interface Sci. 342 (2010) 455–461, https://doi.org/10.1016/j.jcis.2009.10.028.
[28] J.-S. Lim, S.-M. Kim, S.-Y. Lee, E.A. Stach, J.N. Culver, M.T. Harris, Formation of Au/Pd alloy nanoparticles on TMV, J. Nanomater. 2010 (2010) e620505, https://doi.org/10.1155/2010/620505.
[29] C. Moreira Da Silva, N. Ortiz-Peña, L. Boubekeur-Lecaque, J. Dušek, T. Moravec, D. Alloyeau, N.-T. Ha-Duong, In situ insights into the nucleation and growth mechanisms of gold nanoparticles on tobacco mosaic virus, Nano Lett. 23 (2023) 5281–5287, https://doi.org/10.1021/acs.nanolett.3c01311.
[30] B. Bhyravbhatla, S.J. Watowich, D.L.D. Caspar, Refined atomic model of the four-layer aggregate of the tobacco mosaic virus coat protein at 2.4-å resolution, Biophys. J. 74 (1998) 604–615, https://doi.org/10.1016/S0006-3495(98)77819-1.
[31] J. Turkevich, P.C. Stevenson, J. Hillier, A study of the nucleation and growth processes in the synthesis of colloidal gold, Discuss. Faraday Soc. 11 (1951) 55–75, https://doi.org/10.1039/DF9511100055.
[32] Gerald Oster, The isoelectric points of some strains of tobacco mosaic virus, J. Biol. Chem. 190 (1951) 55–59, https://doi.org/10.1016/S0021-9258(18)56044-0.
[33] Y. Zhao, F. Zhou, H. Zhou, H. Su, The structural and bonding evolution in cysteine–gold cluster complexes, Phys. Chem. Chem. Phys. 15 (2013) 1690–1698, https://doi.org/10.1039/C2CP42830J.
[34] S. Pu, C. Gong, A.W. Robertson, Liquid cell transmission electron microscopy and its applications, R. Soc. Open Sci. 7 (2020) 191204, https://doi.org/10.1098/rsos.191204.
[35] T. Couasnon, D. Alloyeau, B. Ménez, F. Guyot, J.-M. Ghigo, A. Gélabert, In situ monitoring of exopolymer-dependent Mn mineralization on bacterial surfaces, Sci. Adv. 6 (2020) eaaz3125, https://doi.org/10.1126/sciadv.aaz3125.
[36] K. Gnanasekaran, H. Chang, P.J.M. Smeets, J. Korpanty, F.M. Geiger, N. C. Gianneschi, In situ Ni2+ stain for liposome imaging by liquid-cell transmission electron microscopy, Nano Lett. 20 (2020) 4292–4297, https://doi.org/10.1021/acs.nanolett.0c00898.
[37] M. Piffoux, N. Ahmad, J. Nelayah, C. Wilhelm, A. Silva, F. Gazeau, D. Alloyeau, Monitoring the dynamics of cell-derived extracellular vesicles at the nanoscale by liquid-cell transmission electron microscopy, Nanoscale 10 (2018) 1234–1244, https://doi.org/10.1039/C7NR07576F.
[38] N.M. Schneider, M.M. Norton, B.J. Mendel, J.M. Grogan, F.M. Ross, H.H. Bau, Electron–water interactions and implications for liquid cell electron microscopy, J. Phys. Chem. C 118 (2014) 22373–22382, https://doi.org/10.1021/jp507400n.
[39] B. Ambrožič, A. Prašnikar, N. Hodnik, N. Kostevšek, B. Likozar, K.Ž. Rožman, S. Šturm, Controlling the radical-induced redox chemistry inside a liquid-cell TEM, Chem. Sci. 10 (2019) 8735–8743, https://doi.org/10.1039/C9SC02227A.
[40] S. Link, M.A. El-Sayed, Size and temperature dependence of the plasmon absorption of colloidal gold nanoparticles, J. Phys. Chem. B 103 (1999) 4212–4217, https://doi.org/10.1021/jp984796o.
[41] J.-W. Park, J.S. Shumaker-Parry, Strong resistance of citrate anions on metal nanoparticles to desorption under thiol functionalization, ACS Nano 9 (2015) 1665–1682, https://doi.org/10.1021/nn506379m.
[42] H.A. Nguyen, I. Jupin, P. Decorse, S. Lau-Truong, S. Ammar, N.-T. Ha-Duong, Assembly of gold nanoparticles using turnip yellow mosaic virus as an in-solution SERS sensor, RSC Adv. 9 (2019) 32296–33237, https://doi.org/10.1039/c9ra08015e.

[43] E. Hao, G.C. Schatz, Electromagnetic fields around silver nanoparticles and dimers, J. Chem. Phys. 120 (2004) 357–366, https://doi.org/10.1063/1.1629280.
[44] E.C. Le Ru, E. Blackie, M. Meyer, P.G. Etchegoin, Surface enhanced Raman scattering enhancement factors: a comprehensive study, J. Phys. Chem. C 111 (2007) 13794–13803, https://doi.org/10.1021/jp0687908.
[45] M. Blanco-Formoso, N. Pazos-Perez, R.A. Alvarez-Puebla, Fabrication and SERS properties of complex and organized nanoparticle plasmonic clusters stable in solution, Nanoscale 12 (2020) 14948–14956, https://doi.org/10.1039/D0NR04167J.